ASSESSING THE SENSITIVITY OF TURBINE CASCADE FLOW TO INFLOW DISTURBANCES USING DIRECT NUMERICAL SIMULATION

R.D. Sandberg
University of Southampton
Southampton, U.K., sandberg@soton.ac.uk

R. Pichler
University of Southampton
Southampton, U.K.

L. Chen
University of Southampton
Southampton, U.K.

ABSTRACT

Direct numerical simulations (DNS) are conducted of flow through a linear low-pressure turbine cascade with T106 blade sections at Re=60,000, based on chord and isentropic exit velocity. A highly efficient in-house compressible Navier-Stokes solver was adapted for turbine cascade simulations and applied to investigate the effect of inflow disturbances on transition behaviour and blade profile losses. It was found that in compressible DNS the attenuation of acoustic reflections at the inflow boundary are essential as the wake loss, unlike the pressure coefficient on the blade, is sensitive to upstream acoustic perturbations.

The results of DNS without inflow turbulence are compared with experimental data and show excellent agreement for both pressure coefficient on the blade and for the wake loss.

Additional DNS with inflow turbulence level Tu=1% and Tu=3.8% were conducted. In all cases a laminar boundary-layer separation on the suction side was observed, however, the separation bubble size varies with turbulence level. It is found that with increasing turbulence level the peak amplitude of the wake loss reduces and the peak location is shifted towards the pressure side, and that the separation point of the suction side boundary layer moves downstream.

INTRODUCTION

To reduce specific fuel consumption and cost of jet engines, it is desirable to decrease the number of blades. This results in the individual blades of modern low-pressure turbines (LPT) being subjected to more severe pressure gradients, which affect the boundary layers. The profile losses of a linear turbine cascade depend strongly on the state of the boundary layers on the blades. Due to high pressure ratios and moderate Mach and Reynolds numbers in LPTs, the boundary layers are prone to laminar separation. Modern turbine blades actually allow for small separation bubbles on the blade surface by design. Both separation bubbles and the type/location of

laminar-turbulent transition type of a boundary layer are known to be sensitive to upstream disturbances. In particular incoming wakes have a profound effect on laminar separation bubbles and boundary layer mechanisms.

In an experimental study, Engber and Fottner [1] investigated the effect of incoming wakes on boundary layer transition of a highly loaded turbine cascade and provided data to improve empirical correlations for the calculation of transition in boundary layers. A later experiment showed a variation of the pressure loss coefficient for different clocking positions of the incoming wakes [2]. The first incompressible direct numerical simulation (DNS) of a turbine cascade was performed by Wu and Durbin [3] and found evidence that incoming wakes are responsible for longitudinal structures forming on the pressure side. Additional numerical studies, also using incompressible DNS and large-eddy simulations (LES) have contributed further to the understanding of the effect of incoming wakes on the pressure and suction side boundary layers [4,5]. In these studies both LES and DNS of the same configuration were compared and it was concluded that good overall agreement with DNS could be obtained with well resolved LES.

Ravery *et al.* [6] conducted compressible LES without incoming background turbulence level and reported on the coupling of the separation bubble and vortex shedding at the trailing edge. Matsuura and Kato [7] performed compressible LES with different inflow background turbulence levels and found that the vortex-shedding separation-bubble coupling was negligible at higher inflow turbulence levels. Sarkar [8] performed incompressible LES focusing on wakes with different eddy structure size and showed that the structure of the incoming wakes, i.e. level of three dimensionality, strongly affects blade performance and wake losses.

In a recent contribution, Medic and Sharma [9] performed compressible LES at various Reynolds number and found significantly improved results compared to URANS. However, despite capturing most trends observed in experiments with LES, at

lower Reynolds number the losses were under predicted for clean inflow cases. In addition, in contrast to available experimental data no significant reduction in wake loss could be found for 4% free stream turbulence level and the boundary layer separation points obtained by LES appeared insensitive to changing freestream levels. One of the main objectives of the current work is therefore to assess whether better agreement with experimental results can be obtained by eliminating the uncertainties introduced by subgrid scales models, i.e. performing fully resolved DNS.

Further, to date most studies have either focused on the influence of background turbulence level [7] or the disturbances caused by incoming wakes. The influence of both effects has been shown to be important in the context of loss prediction. In a real engine environment both background turbulence and wake disturbances coexist with varying respective strengths and so it would be of interest to thoroughly investigate the combined effect, as suggested by Coull and Hodson [10].

In the present paper, a first step towards this goal is made by testing a numerical setup that allows for compressible DNS of a linear LPT cascade with inlet background turbulence using a novel Navier-Stokes code. In this initial step, this setup is used to investigate the influence of inflow turbulence on the blade performance and wake losses. In order to resolve the incoming turbulence, a fine mesh upstream of the blade profile and in the passage is required and therefore no large savings in computational cost using large-eddy simulation over DNS can be expected. The main objectives of the current paper are:

i. validate the numerical setup, i.e. compressible DNS with novel code, against experiments
ii. investigate the effect of inlet turbulence on transition and wake
iii. generate a database of the turbulent kinetic energy transport equation budget for future model improvement

DESCRIPTION OF TEST CASE

The turbine blade geometry considered in the current work is the T106 profile experimentally investigated by Stadtmüller [11]. The measurements were obtained in a low-pressure linear turbine test rig with seven aft-loaded blades with an aspect ratio of 1.76, implying that the flow at the midspan can be considered to be statistically two-dimensional. Therefore, the use of spanwise periodic boundary conditions would appear to be a reasonable assumption. In the experiments, the pitch-to-chord ratio, stagger angle λ, the inlet flow angle β_1 and the exit flow angle β_2 are 0.799, 30.7°, 37.7° and 63.2°, respectively. However, as explained in Michelassi *et al.* [12], there is some uncertainty about the actual inlet conditions, both in terms of total pressure and inlet flow angle. RANS simulations by Stadtmüller

[11] and DNS and LES by Michelassi *et al.* [12] suggest an inlet angle of 45.5°. A variable density system in the test rig allowed measurements at a relatively low Reynolds number of 5.18×10^4 and an isentropic exit Mach number of 0.4. In the current study, the resulting Reynolds number and outlet Mach number were 59,634 and 0.405, respectively. The ratio of specific heats is specified as $\gamma = 1.4$ and the Prandtl number as $Pr = 0.72$. The spanwise width of the computational domain was chosen as 0.2 chord lengths, which is deemed to be sufficient to capture transition in a possibly separated blade boundary layer based on previous experience gained with separation bubbles on low-Reynolds number aerofoils [13]. Furthermore, previous studies of linear turbine cascades found a spanwise width based on axial chord of 0.2 [14, 15] or even 0.15 [3] to be adequate.

NUMERICAL SETUP

The current DNS study was performed with a new in-house multi-block structured curvilinear compressible Navier-Stokes solver purposely developed for exploiting high-performance computing systems [16]. The governing equations were non-dimensionalized by the inlet velocity and the chord, thus all lengths given in the following are normalized with the axial chord.

The numerical method comprises a five-step, fourth-order accurate low-storage Runge-Kutta method [17] for the time integration, state-of-the-art parallelizable wavenumber optimized compact finite differences [18] for the spatial discretization in the streamwise and pitchwise directions and a Fourier method using the FFTW3 library for discretization of the spanwise direction. Additionally, a skew-symmetric splitting [19] is used to stabilize the convective terms. The novel solver has been thoroughly validated by carrying out simulations of Tollmien-Schlichting waves in subsonic boundary layers and oblique instability waves in supersonic boundary layers, matching linear stability results. Also, turbulent boundary layer and pipe flow simulations were conducted, showing good agreement with published data [20, 21]. The code has recently been used for DNS of turbulent supersonic wakes [22] and turbulent jets in coflow [23] for analysis of jet noise. A variant of the code has also been used for extensive studies on separation bubbles on airfoils [13].

For the current study, the flow solver has been modified to handle linear turbine-cascade geometries by allowing the desirable combination of an O-type grid around the turbine blade, enabling adequate resolution at leading and trailing edges, and an H-type grid away from the blade to allow for pitchwise periodic boundary conditions. This was achieved by using characteristic interface conditions [24] to connect the O- and H-type grids with each other as shown in figure 1. In order to study the sensitivity of
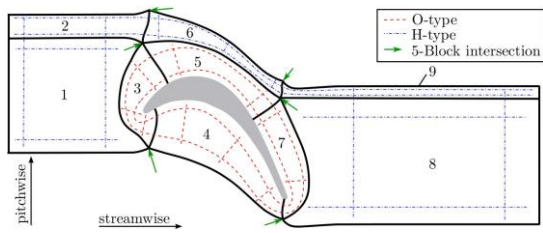
Fig. 1   Combined O-type/H-type grid topology used in the current study.

the linear turbine cascade flow to inflow turbulence, a turbulent inflow generation technique was required. Various methods have been proposed over the years and can be broadly classified into two categories: prescribing real time-dependent flow structures from precursor simulations, databases and recycling approaches [e.g. 25], or the use of physical models [e.g. 26] or artificial/synthetic turbulence [cf 27]. In the digital filter approach by Klein *et al.* [27], a digital filtering operation in all spatial direction is applied to a random number field. To improve numerical efficiency, Xie and Castro [28] modified the original method such that at every time step only a two-dimensional random field is filtered. Data from each time step are correlated with the data from the previous time step by using an exponential function. In addition, in this method the artificially generated turbulent inflow satisfies prescribed integral length scales and Reynolds-stress distributions, making it more suitable for developed turbulent shear flows, a feature not used in the current study, though. Touber and Sandham [29] further extended the synthetic turbulence approach to compressible flows by invoking the strong Reynolds analogy for density fluctuations. In the current work, this method is used in the following procedure: The mean flow profiles to achieve a certain inlet angle and total pressure are specified at the inlet boundary and are superposed with the turbulent fluctuations calculated using the digital filter technique described above. All coefficients used for the digital filter in order to generate quasi isotropic turbulence entering the domain in the final simulations are compiled in table 1. The coefficients were chosen such that the large scales at the inflow would be similar in size to those generated by an upstream blade trailing edge. Preliminary simulations indicated that the digital filter technique is reasonably robust to the choice of filter coefficients.

In an LPT cascade the grid spacing close to the blade (i.e. wall) needs to be sufficiently small to

Velocity component	u	v	w
I_x (in chords)	0.06	0.06	0.08
N_{Fy} (grid points)	30	30	36
N_{Fz} (grid points)	30	30	36

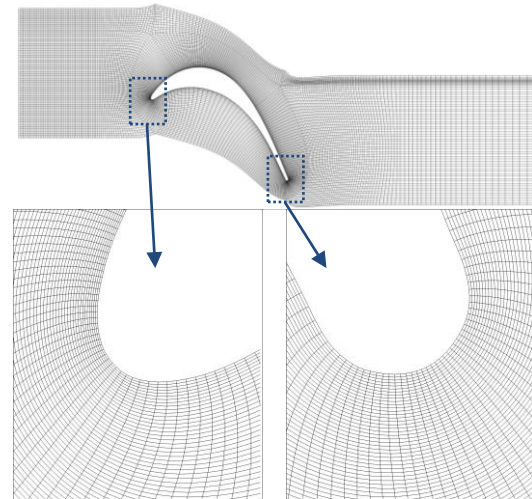**Table 1 Coefficients for digital filter technique [20].**

Fig. 2   Final grid obtained with in-house Poisson-type grid generator (top) – every fourth grid line shown; close-ups of leading and trailing edges (bottom left and right).

resolve the wall structures. On the other hand, the required spacing of the grid away from the wall depends on whether inflow turbulence is imposed but generally can be coarser than in the near-blade region. Due to the round leading and trailing edges of the blade, an O-type grid is the best choice to ensure orthogonal wall next cells along the entire surface. To account for periodicity in the pitchwise direction, an H-type grid is more suitable. Thus the ideal choice for the highest accuracy is a multi-block structured mesh comprising an O-type grid around the blade surrounded by an H-type grid. The grid used here is based on the structure suggested by Gross and Fasel [30] who developed grids particularly suited for cascade simulations. The grid topology is presented in figure 1. Because the grid is periodic in the pitchwise direction the uppermost and lowest lines denote a periodic boundary. The overall setup contains nine blocks, with the number associated with each block given by the black number. The O-type section is comprised of blocks 3, 4, 5 and 7 which can be further decomposed into subdomains (indicated by the red dashed lines). The H-type section is comprised of the remaining blocks, which also can be decomposed in to subdomains (indicated by the blue dash-dotted lines). At the points indicated by arrows, five blocks intersect. At these points the cells cannot be orthogonal but have a maximum angle of 360/5=72 degrees. Since the uppermost and lowest lines are periodic four of these five-block points exist. In the following the method used to generate smooth grids for this topology is explained. The grid is generated following the method of Gross and Fasel [30], which is based on the solution of the Poisson equation. However, several modification to the original method have been made to improve the quality of the grid and increase flexibility in the distribution of points, e.g. the grid can be refined at
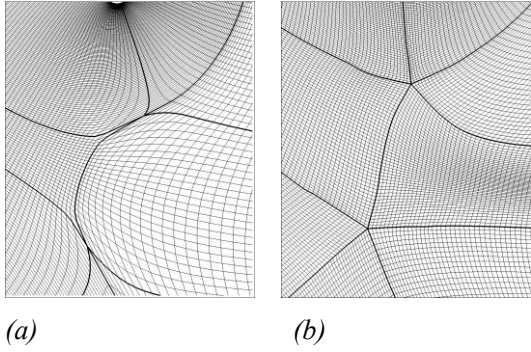
(a)   *(b)*

Fig. 3   **Details of 5-block intersection obtained with original Poisson solver [21] (a) and with modified Poisson solver (b).**

Fig. 4   **Location of first grid point in wall-normal direction in wall units on blade surfaces.**

block boundaries to improve the performance of the characteristic interface conditions connecting the blocks with each other (minimizing spurious pressure reflections from the interfaces). To ensure the best possible accuracy at the 5-block intersections, the maximum angle of 72 degrees per block is enforced. Despite this being the best quality achievable, the grid at the 5-block intersections is non-orthogonal which reduces the accuracy. Thus the modified grid generation process allows for these points to be moved away from regions in which very high accuracy is essential, e.g. in the wake or close to the wall. The final grid generated with the modified Poisson solver, decomposed into the nine blocks discussed above, is illustrated in figure 2. In figure 2, close-ups of the leading and trailing edge regions are also shown, displaying good resolution and nearly orthogonal cells close to the wall. Figure 3 illustrates the considerable improvement in the grid quality at the 5-block interfaces obtained by adding a special treatment at these points to the original Poisson-type solver [30]. The left-hand figure shows one 5-block intersection generated with the original method, displaying highly skewed cells. The right-hand figure shows a 5-block interface generated enforcing a 72 degree angle for each block and with user-control of grid clustering at the interface, resulting in a good quality mesh at the block interfaces.

Block	$N_x \times N_y$	$Np_x \times Np_y$
1	288×192	12×8
2	288×48	12×2
3	144×192	6×8
4	144×240	6×10
5	144×240	6×10
6	48×240	2×10
7	144×192	6×8
8	288×192	12×8
9	288×48	12×2
total	274,176	476

Table 2 Number of grid points (N) and the number of processors (Np) for each block in the computational domain (see figure 1) in the streamwise (x) and pitchwise (y) directions for case with *Re*=60,000.
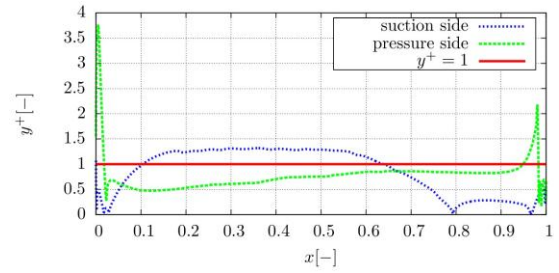
The number of grid points and number of subdomains in the streamwise (x) and pitchwise (y) directions for each block are given in table 2. In the spanwise direction 32 Fourier modes were employed with 100% de-aliasing (using 66 collocation points in physical space), resulting in a total of 18.1×10^6 grid points for each simulation. The number of grid points along the surface of the blade is 864 points and in the wall normal direction the spacing is nearly constant around the blade with $\Delta y \sim 0.0028$. In order to check whether the resolution is sufficient, the grid cell size was scaled in wall-coordinates with the local wall shear-stress τ_w. The local resolution in wall coordinates is shown in figure 4. The first wall-normal grid point on the suction side is located at $\Delta y^+ > 1$ for a substantial amount of the chord. However, the maximum value is below 1.4 which, using the wave-number optimized compact scheme, is comparable to values well below the required value of unity with a standard fourth-order scheme. Furthermore, in the region of values exceeding unity the boundary layer is laminar and the resolution is deemed sufficient with roughly 30 points across the boundary layer. On the pressure side the wall-normal resolution is even better, except close to the trailing edge, where Δy^+ reaches 2.5, albeit here again the boundary layer is laminar. The resolution in the streamwise and spanwise directions are obtained by multiplying Δy^+ with the aspect ratios of the cells at the wall, giving values of $\Delta x^+ < 10$ and $\Delta z^+ < 11$. These values are similar to the values used in the DNS by Michelassi *et al.* [12], in particular considering the considerably higher accuracy of the wave-number optimized compact scheme in the streamwise and pitchwise directions, and the spectral method in the spanwise direction. Therefore, the grid resolution is considered to be adequate to fully resolve the flow. With the grid described above, a nondimensional timestep of $\Delta t = 5 \times 10^{-5}$ was specified in order to satisfy the numerical stability requirement of a CFL number of less than unity.
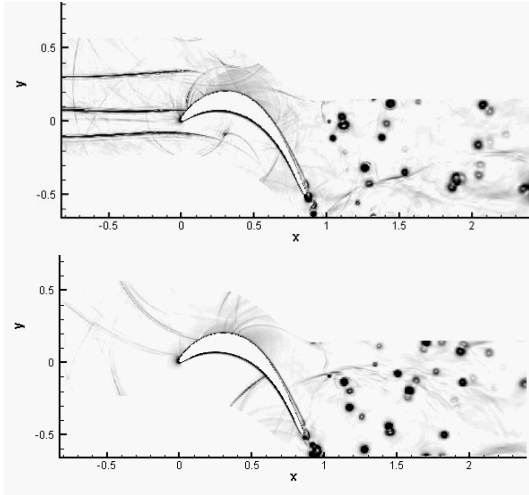
Fig. 5 **Instantaneous contours of streamwise density gradient from precursor 2D simulations without (top) and with (bottom) sponge zone at inlet boundary.**

One major difference between the current DNS work to previous DNS studies [e.g. 12] is the use of a compressible solver, which also explicitly resolves the acoustic field. This represents an additional challenge on the boundary conditions to not generate spurious reflections, in particular at the inlet and outlet which artificially truncate the physical flow field. At the outlet boundary a characteristic boundary condition is employed. At the inlet boundary, initially a fixed boundary condition was used in order to impose particular inlet conditions, i.e. total pressure and inlet angle. This, however, causes considerable reflections of the acoustic waves generated by scattering at the trailing and leading edges. In order to avoid the acoustic reflections at the inlet boundary, initially a characteristics-based approach was considered. However, when the boundary condition was set to be fully non-reflective, the inlet angle, one of the crucial parameters, could not be maintained. Using a correction to the characteristic boundary condition to avoid a drift of the inlet flow variables following an approach similar to that proposed by Poinsot and Lele [31] comes at the price of loss of perfectly non-reflective properties. The acoustic
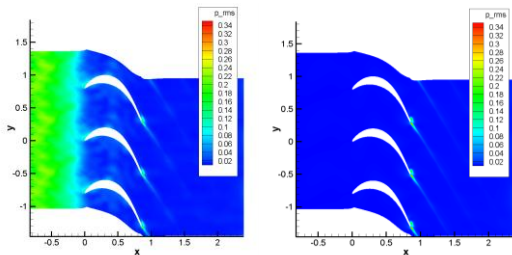

Fig. 6 **Contours of root-mean-square pressure from precursor 2D simulations without (left) and with (right) sponge zone at inlet boundary.**
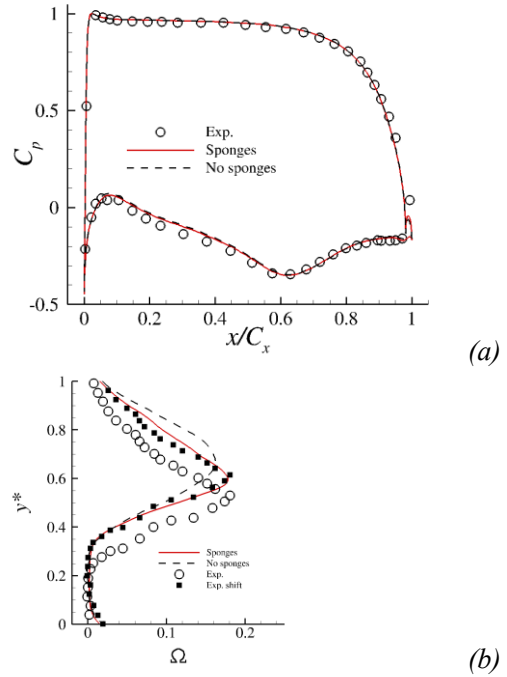

(a)

(b)

Fig. 7 **Pressure coefficient (a) and wake loss (b) obtained from simulations with and without sponge layer at inlet.**

reflections occurring in that case, albeit reduced in amplitude when compared to the fixed inlet boundary condition, over time result in an accumulation of high amplitude waves parallel to the pitchwise boundaries travelling in the pitchwise direction in the inlet region, as seen in figure 5 (top). Although one might suspect that these acoustic waves propagating in the pitchwise direction through the inlet region only will not affect the overall solution, figures 6 and 7 show that this is not the case. In figure 6, root-mean-square pressure amplitudes of up to 0.2 can be seen in the inlet region when the inlet reflections are not explicitly treated.

Therefore, a sponge layer, based on adding a dissipation term to the right-hand side (RHS) of the governing equations, forcing the flow solution to a target state [32], was implemented. The forcing term added to the RHS has the following form: $f\sigma_0(q - q_{target})$, where f is a ramping function that takes values of 1 at the inlet boundary and 0 in the field, q denotes the conservative variable vector, q_{target} are the values the solution is driven to, and σ_0 is a free parameter, set to 0.02 in the current work. Using the inflow sponge, which is only applied in the region $-0.82 \leq x \leq -0.77$, i.e. from the inlet boundary to 0.05 chord lengths downstream, the spurious waves traveling in the pitchwise direction are removed. This can be clearly observed in figure 5 (bottom), showing that only acoustic waves traveling upstream from the cascade are present. Figure 6 (right) illustrates that the inflow region now is 'clean' also in a statistical sense.
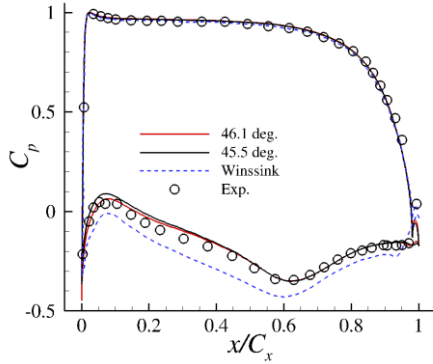
Fig. 8 Pressure coefficient on blade compared with experiments [11] and incompressible reference DNS [14].

Fig. 9 Wake loss compared with experiments [11].

It is worth noting that looking at the c_p distribution on the blade alone can be deceiving, as illustrated by figure 7, where no noticeable difference in the c_p distribution can be discerned for cases with and without inlet sponge. The pressure coefficient is defined as $c_p(x) = (p_s(x) - p_{out})/(p_{t,in} - p_{out})$, where $x, p_{t,in}, p_s(x)$ and p_{out} are the non-dimensional axial chord, mass-averaged stagnation pressure at inlet, static pressure along the blade and the mass averaged static pressure at the outlet measurement plane 40% chord downstream of the trailing edge, respectively. When focusing the attention on the wake loss, it appears that the artificial waves present in the case without inlet treatment considerably alter the wake loss profile, making it fuller than the one obtained from the case with sponge, which agrees considerably better with the reference data. The wake loss is defined as $\Omega(y) = (p_{t,in} - p_t(y))/(p_{t,in} - p_{out})$, with $p_t(y)$ the stagnation pressure along the non-dimensional pitchwise taken at 40% chord downstream of the trailing edge.

All cases discussed in the current paper were initialized and run for several flow-through times in two dimensions. Once a time-periodic state was achieved, an instantaneous two-dimensional solution was extruded in the spanwise direction (using a spectral approach, the 2D solution was prescribed as the zeroth mode and higher modes with zero amplitude were appended) and continued. The full three-dimensional DNS were then run for 10 flow-through times before accumulating statistical data over an additional 10 flow-through times, ensuring converged statistics. As shown in table 2, the computational grid was divided into 476 subdomains, each constituting an MPI process. For three-dimensional simulations, the spanwise direction was further parallelized using OMP threads, selecting between 2 and 8 OMP threads, thus running on a total number of up to 3808 cores, enabling a turnaround of less than 24 hours wall time on a CRAY XE6 from an initial 2D simulation to fully converged statistics.
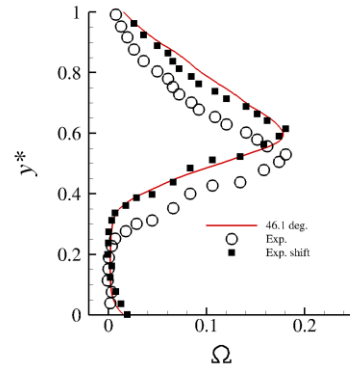
VALIDATION

Having made a number of modifications to the original flow-solver in order to compute flow through an LPT cascade, a thorough validation is required. To that end, DNS were conducted with a clean inlet, i.e. no inlet turbulence was specified, at a Reynolds number of Re=60,000 and exit Mach number of M=0.4, and the results compared with reference data [6]. The pressure coefficient on the blade obtained from the current DNS using two slightly different inlet angles, 45.5° and 46.1°, is compared to the experimental results [11] and the incompressible DNS of Wissink *et al.* [14] in figure 8. As expected, varying the inlet angle does not significantly affect the c_p distribution on the pressure side and excellent agreement with the reference data is obtained. On the suction side, varying the inlet angle does affect the results, with the inlet angle of 46.1° resulting in the best agreement with the experimental data. The difference between both angles in mainly confined to the region close to the leading edge, with the location of the suction peak being very similar for either case. It is noteworthy that the results obtained with the compressible DNS code nearly coincide with the experimental data on the suction side, unlike the results from the incompressible DNS in which the shape of the c_p distribution roughly matches the experiments but the suction peak is located too far upstream and the amplitude is overpredicted significantly.

In figure 9, the wake loss obtained from the compressible DNS with inlet angle 46.1° is compared to the reference data. Comparing the DNS results with the raw experimental data suggests good agreement in shape, despite a shift in the pitchwise direction. If the experimental data are shifted in the pitchwise direction until the peaks of the DNS and experimental data are aligned, the DNS data show a surprisingly good agreement with the experimental data, demonstrating the ability of DNS to accurately capture the physics. Note that the pitchwise shift of the experimental data is considered to be justified in
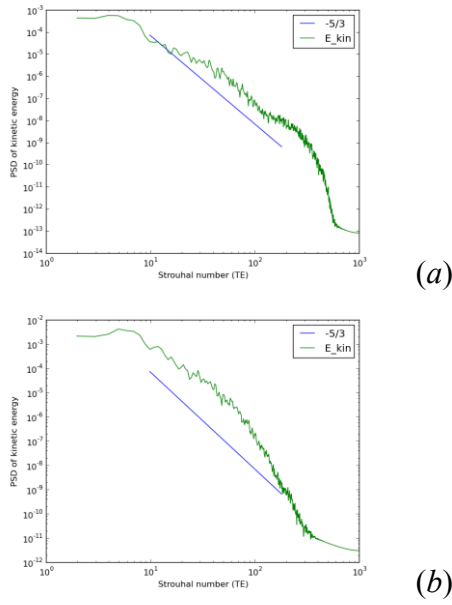
(a)

(b)

Fig. 10 Kinetic energy spectrum (Tu=3.8% case) at the location: (*a*) upstream (x=-0.3, y=0) and (*b*) wake (x=1.25, y=-0.32).

light of the exact measurement position not being known. Given the good agreement with experiments in both blade pressure coefficient and wake loss, for all simulations presented from here on the inlet angle is set to 46.1°.

As a final step, an additional DNS was performed using a finer mesh. Although this simulation was performed at the time when a characteristic approach was chosen at the inflow boundary and the angle was set to 45.5°, the result were virtually undistinguishable from the DNS on the coarser grid using the same set-up, confirming that the DNS are grid converged. The results presented so far give confidence in the ability of the novel compressible code HiPSTAR to accurately represent the compressible flow through the linear LPT cascade, and thus the DNS study of the effect of inflow turbulence level could be performed.

RESULTS

The objective of the current paper is to investigate the effect of inflow turbulence on the flow through the LPT cascade using compressible DNS. We consider three typical cases with different turbulence intensities at the inlet of the passage (x=-0.3), i.e. clean (*Tu*=0%), *Tu*=1.1% and *Tu*=3.8%.

Three dimensional simulations are restarted from fully developed 2D results. After about 10 pass through time, to avoid the transient period, samples have been collected for another 10 pass through times to obtain statistically meaningful turbulence properties. The kinetic energy spectra obtained from the *Tu*=3.8% case in the upstream and wake region are shown in figures 10(*a*) and 10(*b*), respectively. The kinetic energy spectra upstream the blade and in
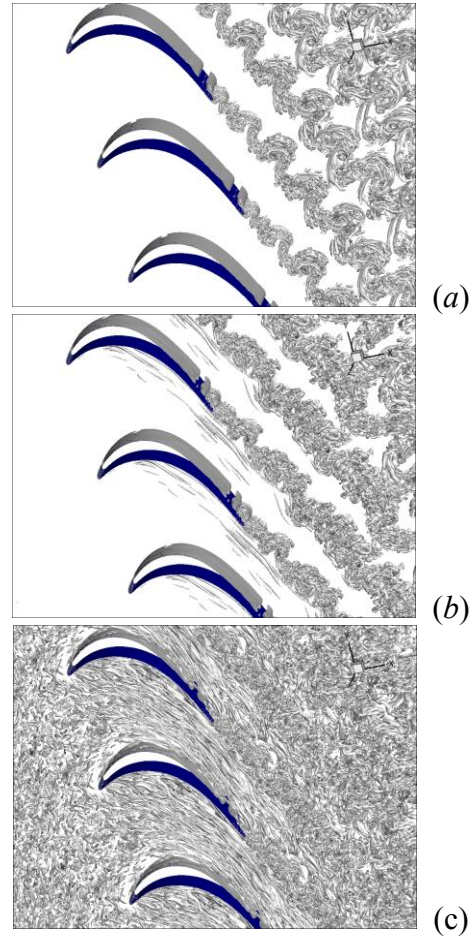

(a)

(b)

(c)

Fig. 11 Instantaneous iso-surfaces of the second invariant of the velocity-gradient tensor, *Q*=8, for (a) clean, (b) *Tu*=1.1% and (c) *Tu*=3.8% cases.

the wake seem to reach an inertial sub-range, reasonably close to a $k^{-5/3}$ scaling, with the Strouhal number scaled on trailing-edge thickness. The spatial spectra can be approximately obtained using Taylor's hypothesis which is limited to homogeneous turbulence with small turbulence intensity. The illustrated slope indicates that the present calculation may reliably simulate the energy cascade behavior and gives further evidence that the simulations are adequately resolved.

In figure 11 instantaneous iso-surfaces of the second invariant of the velocity-gradient tensor are shown to give a qualitative impression of the flow for the three cases with varying inflow turbulence level. In the clean case, laminar flow separation in the aft section of the suction side can be observed with highly spanwise coherent vortex shedding. The wake developing downstream of the trailing edge also appears very organized in the clean case.

For a turbulence level of *Tu*=1.1%, the iso-surfaces of *Q* on the blade surface are similar to the clean case, however, the wake looks less organized and streamwise elongated structures are present in the passage. These structures are presumably generated
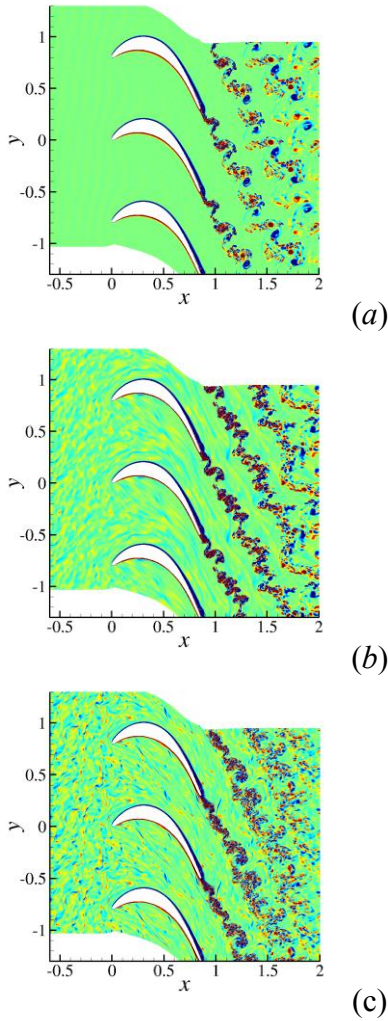
Fig. 12 Instantaneous contours of the spanwise vorticity component, for (a) clean, (b) *Tu*=1.1% and (c) *Tu*=3.8% cases.

by streamwise stretching of the isotropic turbulence structures generated at the inflow by the strong acceleration of the flow in the passage. For the case with *Tu*=3.8%, stronger spanwise modulation of the separated shear layer is observed and the wake shows even less spanwise coherence. For this case, the change of the turbulence structure from nearly isotropic upstream of the blades to predominantly longitudinal structures in the passage can be seen.

The differences in spanwise coherence of the wake structures for varying inflow turbulence level can be more clearly seen when looking at instantaneous contours of the spanwise vorticity component, shown in figure 12.

For a more quantitative assessment of the effect of inflow turbulence level on the blade performance, the pressure coefficient c_p, is compared to experimental data in figure 13. A zoom-in view near the trailing edge shows the differences of the pressure distribution for different turbulence intensities. Downstream of x/C_x=0.6, the boundary layer on the suction side experiences a favorable pressure gradient
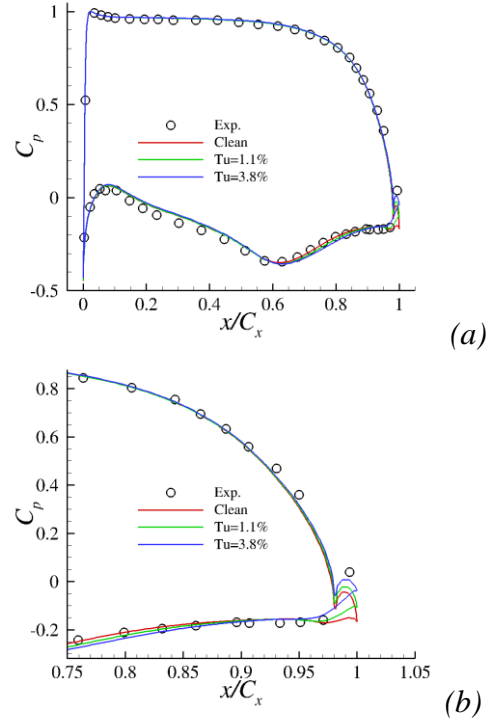

Fig. 13 Pressure coefficients on the blade surface (a) for three cases compared with (clean) experiments [11], zoom-in of trailing edge region (b).

and the pressure grows until reaching a value that varies minimally going further downstream, a behavior indicative of a flow separation. From x/C_x~0.95, the pressure for the clean case remains flat, suggesting that the boundary remains separated until the end of the blade. In contract, in the cases with turbulent inflow, the pressure recovers before the trailing edge implying that the boundary layer reattaches. For the *Tu*=3.8% case, reattachment appears to occur further upstream with pressure rising to a larger value.

Figure 14 shows the distributions of the skin-friction coefficient τ_w on the blade surface. Overall, it appears as if the results for all three cases collapse over most of the blade. However, a zoom-in of the trailing edge region reveals significant differences. It can be identified that for the clean case, the boundary layer separates at about x/C_x=0.8 and reattaches at x/C_x=0.97. With increasing turbulence intensity the separation is delayed and the *Tu*=3.8% case exhibits flow separation at x/C_x=0.84. However, looking at figure 14 (b) in both cases with turbulent inflow the boundary layer does not appear to reattach, despite showing the same behavior and similar (positive) slope just upstream of x/C_x=0.95. Were the two cases to reattach a shorter, smaller, recirculation region would be the consequence. In subfigure (c), the skinfriction for x/C_x≥0.95 is shown. Here it can be observed that the flow separation on the pressure side of the trailing-edge is similar in all cases but that
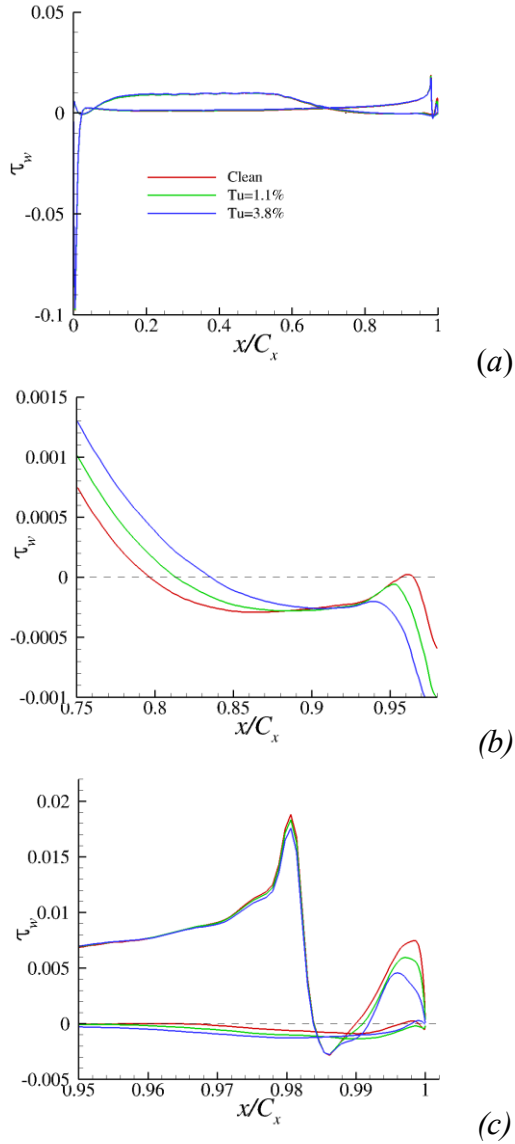
(a)

(b)

(c)

Fig. 14 Mean skin-friction coefficients for the three cases (a) and a zoom-in view of the trailing-edge region (b-c).

reattachment moves downstream for increasing turbulence level. This presumably affects the suction side and possibly prevents the separated shear layer from reattaching in the cases with turbulent inflow.

Figure 15 illustrates the total pressure losses measured at $x=1.26$, i.e. 40% chord downstream of the TE for the three cases. The coordinate y^* is a normalized scale in the pitchwise direction from the suction to the pressure side, defined as $y^* = (y - y_{max})/(y_{max} - y_{min})$. As shown earlier, the clean case matches the experiment result very well. It can be clearly seen that the peak values of the wake loss for the turbulent inflow cases are lower than in the clean case. Also, the locations of the peaks for the turbulent cases are closer to the pressure side. This can be explained by the change of the suction side
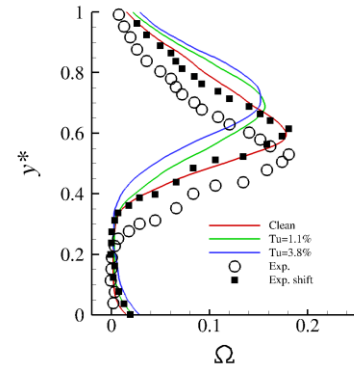

Fig. 15 Wake losses for varying inflow turbulence level *Tu* compared with experiment.

separation bubble for the turbulent cases which leads to a different defect of the wake.

In figure 16 the pitchwise maximum of the compressible turbulence kinetic energy (TKE) in the wake region is shown against the streamwise direction. In all cases, TKE rises quickly from zero at the trailing edge to a peak at roughly 10% axial chord downstream of the blade. The very high levels of TKE obtained at the peak location are due to the laminar-turbulent transition of the wake. An important result is the considerably higher peak value of TKE for the clean case, presumably caused by the significantly higher spanwise coherence of the wake structures, as also observed qualitatively in figures 11
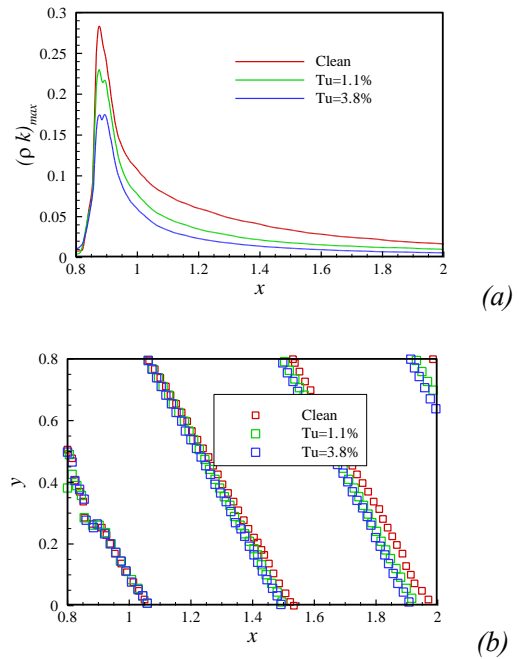

(a)

(b)

Fig. 16 Pitchwise maximum of turbulence kinetic energy in wake over streamwise direction (a) and pitchwise location of maximum turbulence kinetic energy in wake (b).

and 12. In the cases with non-zero inflow turbulence level, the peak value of TKE decreases for increasing *Tu*, due to the initial wake being more strongly perturbed in the spanwise direction and the wake structures that for as a consequence of the Kelvin-Helmholtz instability being less spanwise coherent. In future work, the spanwise coherence function for all cases will be processed and evaluated to assess the validity of this statement.

In addition to the peak TKE values, the pitchwise location of the maximum TKE is plotted over streamwise distance in figure 16. The location of the maximum TKE differs between the three cases, with the peak location of TKE moving towards the pressure side for increasing turbulence level, in line with the results observed in terms of wake losses. The location of the maximum TKE, affecting the angle of the wake, is particularly important in the study of multistage problems, as the pitchwise distribution of TKE can affect transition on the next stage and wake/blade interaction noise.

Many turbulence models are based on the eddy viscosity assumption as well as on the compressible turbulence kinetic energy transport equation (for example in Wilcox [33]). Since the results show good quantitative agreement with experiments and in DNS all scales of turbulence are resolved, and all fluctuation data are available, results can be compared against ones obtained using turbulence models. Therefore, a database is generated containing the full budget of the individual terms in the TKE transport equation. The terms computed and stored are summarized in table 3 using index notation for convenience, with i and j ranging from 1 to 3. All variables have their usual meaning and t_{ji} is the molecular stress tensor.

$\overline{\rho \widetilde{u_i} \widetilde{u_j}}$	Reynolds stress components
$\overline{\rho \widetilde{u_i} \widetilde{u_j}} \dfrac{\partial \widetilde{u_i}}{\partial x_j}$	Production term
$\overline{t_{ji} \dfrac{\partial u_i''}{\partial x_j}}$	Dissipation
$\dfrac{\partial}{\partial x_j} \overline{t_{ji} u_i''}$	Gradient molecular diffusion
$\dfrac{\partial}{\partial x_j} \overline{\rho u_j'' \dfrac{1}{2} u_i'' u_i''}$	Turbulent transport of TKE (triple correlation)
$\dfrac{\partial}{\partial x_j} \overline{p' u_i''}$	Pressure-velocity fluctuation gradient
$\overline{u_i'' \dfrac{\partial P}{\partial x_i}}$	Pressure work
$\overline{p' \dfrac{\partial u_i''}{\partial x_i}}$	Pressure Dilatation

Table 3: TKE transport equation terms

CONCLUSIONS

Compressible direct numerical simulations using a novel in-house high-performance Navier-Stokes solver have been performed of flow through a linear low-pressure turbine cascade with T106 blade sections.

In the current study, a combined O-type/H-type grid topology is used in which the O-grid around the blade is connected to the H-grid via characteristic interface conditions. It is demonstrated that improvements to an existing Poisson-type grid generation tool ensure good mesh quality around the blade, in the wake and at block interfaces. It is also demonstrated that appropriate treatment of the boundaries, in particular the inflow boundary is essential when using compressible DNS as spurious pressure waves, caused by inflow boundary reflections can affect the results. Although c_p does not appear to be strongly affected by changes in the inflow boundary condition, in particular the wake losses show considerable sensitivity to upstream acoustic boundary reflections.

The compressible DNS results of the clean case are compared with experimental data and show excellent agreement, not only for the pressure coefficient on the blade but also for the wake loss, which in the past has been the more difficult quantity to match.

Additional DNS with inflow turbulence level *Tu*=1.1% and *Tu*=3.8% were conducted. In all cases a laminar boundary-layer separation on the suction side was observed, however, the separation bubble size varied with turbulence level. Unlike previous LES studies, using DNS it was found that increasing turbulence level reduces the peak amplitude of the wake loss and shifts the pitchwise peak location towards the pressure side. Also, the separation point of the boundary layer on the suction side was found to move downstream with increasing turbulence level. These results demonstrate that fully resolved DNS can accurately capture the compressible flow in an LPT and the data generated will be valuable for further study of how freestream turbulence affects the aft flow separation and wake development.

NOMENCLATURE

β_1	=	Inlet flow angle
β_2	=	Outlet flow angle
Δt	=	Time step
$\Delta x^+, \Delta y^+, \Delta z^+$	=	Coordinates in wall units
λ	=	Stagger angle
ρ	=	Density
σ_0	=	Coefficient for sponge layer
τ_w	=	Skinfriction coefficient
Ω	=	Wake loss coefficient
c_p	=	Pressure coefficient
C_x	=	Axial chord length
f	=	Ramping function of the sponge
I_x	=	Length scale of inflow turbulence
k	=	Turbulence kinetic energy
Ma	=	Mach number
N	=	Number of grid points

N_p	=	Number of processors
p_{out}	=	Mass averaged static pressure at outlet measurement plane 40% chord downstream of trailing edge
$p_s(x)$	=	Static pressure along blade
$p_t(y)$	=	Static pressure across the wake
$p_{t,in}$	=	Mass-averaged stagnation pressure at inlet
q	=	Conservative variable vector
q_{target}	=	Target values for sponge layer
Q	=	second invariant of the velocity-gradient tensor
Re	=	Reynolds number
St	=	Strouhal number
Tu	=	Turbulence intensity level
x, y, z	=	Streamwise, pitchwise and spanwise coordinates
y^*	=	Normalized scale in the pitchwise direction
y^+	=	Location of first grid point in the wall-normal direction in wall units on blade surfaces

REFERENCES

[1] Engber, M., Fottner L. 1996 "The effect of incoming wakes on boundary layer transition of a highly loaded turbine cascade" AGARD CONFERENCE PROCEEDINGS, 21-1 – 21-11

[2] Heinke, W., Konig, S., Matyschok, B., Stoffel, B., Fiala, A., Heinig, K. 2004 "Experimental investigations on steady wake effects in a high-lift turbine cascade." *Experiments in Fluids* 37, 488-496.

[3] Wu, X., Durbin, P.A. 2001 "Evidence of longitudinal vortices evolved from distorted wakes in a turbine passage." *J. Fluid Mechanics* 446, 199-228.

[4] Michelassi, V., Wissink, J.G., Frohlich, J. Rodi, W. 2003 "" Large-Eddy simulation of flow around low-pressure turbine blade with incoming wakes", *AIAA J.*, Vol.41, No.11 2143-2156

[5]. Wissink, J.G., Rodi, W., Hodson, H.P. 2006 "The influence of disturbances carried by periodically incoming wakes on the separating flow around a turbine blade " *Int. J. Heat Fluid Flow*, 27, 721-729.

[6] Raverdy, B., Mary, I., and Sagaut, P., 2003 "High-Resolution Large-Eddy Simulation of Flow Around Low-Pressure Turbine Blade Introduction," *AIAA Journal*, 41, 3.

[7] Matsuura, K., 2006 "Large-eddy simulation of compressible transitional cascade flows with and without incoming free-stream turbulence," *JSME International Journal Series B*, 49, 3.

[8] Sarkar, S., 2009 "Influence of wake structure on unsteady flow in a low pressure turbine blade passage," *J. of Turbomachinery*, 131.

[9] Medic, G. and Sharma, O. P., 2012 "Large-Eddy Simulation of Flow in a Low-Pressure Turbine Cascade," in *Proc. ASME Turboexpo*, GT2012-68878, 1–10.

[10] Coull, J. D. and Hodson, H. P., 2011 "Unsteady boundary-layer transition in low-pressure turbines," *J. Fluid Mech.*, 681, 1, 370–410.

[11] Stadtmüller, P. 2001 "Investigation of Wake-Induced Transition on the LP Turbine Cascade T106 A-EIZ," DFG-Verbundprojekt Fo 136/11, Version 1.0, University of the Armed Forces Munich, Germany.

[12] Michelassi, V., Wissink, J. and Rodi, W. 2002 "Analysis of DNS and LES of Flow in a Low Pressure Turbine Cascade with Incoming Wakes and Comparison with Experiments," *Flow Turbul. Combust.* 69, 295-330.

[13] Jones, L.E., Sandberg, R.D., Sandham, N.D. 2010 "Stability and Receptivity Characteristics of a Laminar Separation Bubble on an Aerofoil." *J. Fluid Mech.*, Vol. 648, 2010, 257-296

[14] Wissink, J.G. 2003 "DNS of separating, low Reynolds number flow in a turbine cascade with incoming wakes," *Int. J. Heat Fluid Fl.*, 24 (4), 626–635.

[15] Kalitzin, G., Wu, X. and Durbin, P. A., 2003 "DNS of fully turbulent flow in a LPT passage," *Int. J. Heat Fluid Fl.*, 24, 4, 636–644.

[16] CRAY Centre of Excellence Project report 2011:http://www.hector.ac.uk/coe/pdf/HiPSTAR_OMP_Report.pdf

[17] Kennedy, C., Carpenter, M. and Lewis, R. 2000 "Low-storage, explicit Runge-Kutta schemes for the compressible Navier-Stokes equations." *Applied Numerical Mathematics,* 35, 177-219.

[18] Kim, J.W. and Sandberg, R.D., 2012 "Efficient Parallel Computing with Compact Finite Difference Schemes," *Computers and Fluids,* 58, 70-87.

[19] Kennedy, C. and Gruber, A. 2008 Reduced aliasing formulations of the convective terms within the Navier-Stokes equations for a compressible fluid. *J. Comp. Phys.* 227, 1676-1700

[20] Spalart, P. R. 1988 "Direct simulation of a turbulent boundary layer up to Re_θ=1410," *J. Fluid Mech.* 187, 61–98.

[21] Wu, X. and Moin, P. 2008 "A direct numerical simulation study on the mean velocity characteristics in turbulent pipe flow", *J. Fluid Mech.* 608, 81–112.

[22] Sandberg, R.D. 2012 "Numerical investigation of turbulent supersonic axisymmetric wakes" *J. Fluid Mech.*, Vol. 702, 2012, 488-520.

[23] Sandberg, R.D. 2012 Suponitsky, V. and Sandham, N.D., "DNS of compressible pipe flow exiting into a coflow," *Int. J. Heat Fluid Fl.*, 35, 33-44.

[24] Kim, J., Lee, D. 2003 "Characteristic Interface Conditions for Multiblock High-Order Computation on Singular Structured Grid." *AIAA J.* 41 (12).

[25] Lund, T., Wu, X. and Squires, K. 1998 "Generation of turbulent inflow data for spatially-developing boundary layer simulations",. *J. Comput. Phys.* 140 (2), 233–258.

[26] Sandham, N., Yao, Y. & Lawal, A. 2003 "Large-eddy simulation of transonic flow over a bump*," Int. J. Heat Fluid Fl.,* 24, 584–595.

[27] Klein, M., Sadiki, A. and Janicka, J. 2003 "A digital filter based generation of inflow data for spatially developing direct numerical or large eddy simulations*". J. Comput. Phys.* 186 (2), 652–665.

[28] Xie, Z. and Castro, I. 2008 "Efficient generation of inflow conditions for large-eddy simulation of street-scale flows," *Flow Turbul. Combust.* 81 (3), 449–470.

[29] Touber, E., Sandham, N. 2009 "Large-eddy simulation of low-frequency unsteadiness in a turbulent shock-induced separation bubble." *Theor. and Comp. Fluid Dynamics* 23 (2), 79-107.

[30] Gross, A. and Fasel, H. F. 2008 "Multi-block Poisson grid generator for cascade simulations," *Math. and Computers in Simulation* 79 (3), 416–428.

[31] Poinsot, T J and Lele, S K 1992 "Boundary Conditions for Direct Simulations of Compressible Viscous Flows," *J. Comp. Phys.* 101 (1), 104–129.

[32] Freund, J., 1997 "Proposed Inflow/Outflow Boundary Condition for Direct Computation of Aerodynamic Sound," *AIAA J.*, 35(4), 740-742.

[33] Wilcox, D.C. 1998, "Turbulence modeling for CFD," DCW industries La Canada, CA.